Water Splitting with an Enhanced Bifunctional Double Perovskite

Jian Wang,[†] Yang Gao,[†] Dengjie Chen,*[,‡] Jiapeng Liu,[†] Zhenbao Zhang,[‡] Zongping Shao,[§] and Francesco Ciucci*[,†,∥]

[†]Department of Mechanical and Aerospace Engineering, The Hong Kong University of Science and Technology, Hong Kong, China
[‡]Department of Chemistry, Jinan University, Guangzhou 510632, China
[§]State Key Laboratory of Materials-Oriented Chemical Engineering, College of Chemistry & Chemical Engineering, Nanjing Tech University, Nanjing 210009, China
[∥]Department of Chemical and Biological Engineering, The Hong Kong University of Science and Technology, Hong Kong, China

Ⓢ *Supporting Information*

ABSTRACT: The rational design of highly active and durable electrocatalysts for overall water splitting is a formidable challenge. In this work, a double perovskite oxide, i.e., $NdBaMn_2O_{5.5}$, is proposed as a bifunctional electrode material for water electrolysis. Layered $NdBaMn_2O_{5.5}$ demonstrates significant improvement in catalyzing oxygen and hydrogen evolution reactions (OER and HER, respectively), in contrast to other related materials, including disordered $Nd_{0.5}Ba_{0.5}MnO_{3-\delta}$ as well as $NdBaMn_2O_{5.5-\delta}$ and $NdBaMn_2O_{5.5+\delta}$ ($\delta < 0.5$). Importantly, $NdBaMn_2O_{5.5}$ has an OER intrinsic activity (~24 times) and a mass activity (~2.5 times) much higher than those of the benchmark RuO_2 at 1.7 V versus the reversible hydrogen electrode. In addition, $NdBaMn_2O_{5.5}$ achieves a better overall water splitting activity at large potentials (>1.75 V) and catalytic durability in comparison to those of Pt/C−RuO_2, making it a promising candidate electrode material for water electrolyzers. The substantially enhanced performance is attributed to the approximately half-filled e_g orbit occupancy, optimized O p-band center location, and distorted structure. Interestingly, for the investigated perovskite oxides, OER and HER activity seem to be correlated; i.e., the material achieving a higher OER activity is also more active in catalyzing HER.

KEYWORDS: *water splitting, perovskite oxide, layered structure, electronic structure, lattice distortion*
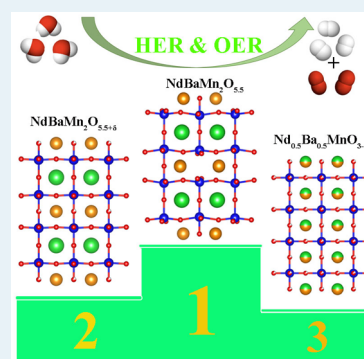
1. INTRODUCTION

According to the International Energy Agency, the global energy demand is projected to increase from 18 TW in 2013 to 26 TW in 2040, because of rapid population growth and industrial expansion.[1] The corresponding increase in carbon dioxide emission will reach 44 Gt/year. These environmental concerns have triggered a focus on sustainable energy sources to mitigate the energy crisis and environmental damage caused by burning fossil fuels, which still account for ~80% of today's power production.[1] However, the effective utilization of the most abundant renewables (e.g., solar and wind) is difficult because of their intermittent nature. As a consequence, sustainable, efficient, and economically viable energy conversion and storage devices are urgently needed. The efficiency of many such devices, including regenerative fuel cells, rechargeable metal−air batteries, and water electrolyzers, is heavily dependent on the electrolysis of H_2O.[2,3] Therefore, developing highly active and durable electrocatalysts for the $H_2O−H_2−O_2$ cycle is the key to accelerating the practical use of many renewable energy technologies.

The oxygen evolution reaction (OER) and hydrogen evolution reaction (HER) are two crucial half-reactions for overall H_2O splitting, which, because of the abundance of water, is considered as the most promising method for the production of high-purity H_2. However, because of the sluggish kinetics of OER and HER, large overpotentials against the theoretical thermodynamic potential [1.23 V vs the reversible hydrogen electrode (RHE)] are usually required to drive H_2O electrolysis. The state-of-the-art catalysts for OER and HER are based on precious metals, e.g., IrO_2 and RuO_2 for OER and Pt metal and its alloys for HER. Precious metals are, however, prohibitively costly. As a result, intense research efforts have focused on earth-abundant metal-based materials. Those include transition metal oxides and hydroxides for OER in basic electrolytes[4,5] and transition metal carbides, nitrides, sulfides, and phosphides for HER in acidic media.[6−9] For the sake of simplifying the configuration and saving money, bifunctional electrode materials for both OER and HER are being pursued.[10,11]

Among various non-precious metal-based catalysts, perovskite oxides are gaining an increasing amount of attention because of their low cost, compositional flexibility, and high intrinsic activity.[12,13] The catalytic activity of perovskite oxides can be improved intrinsically or extrinsically. In reference to the
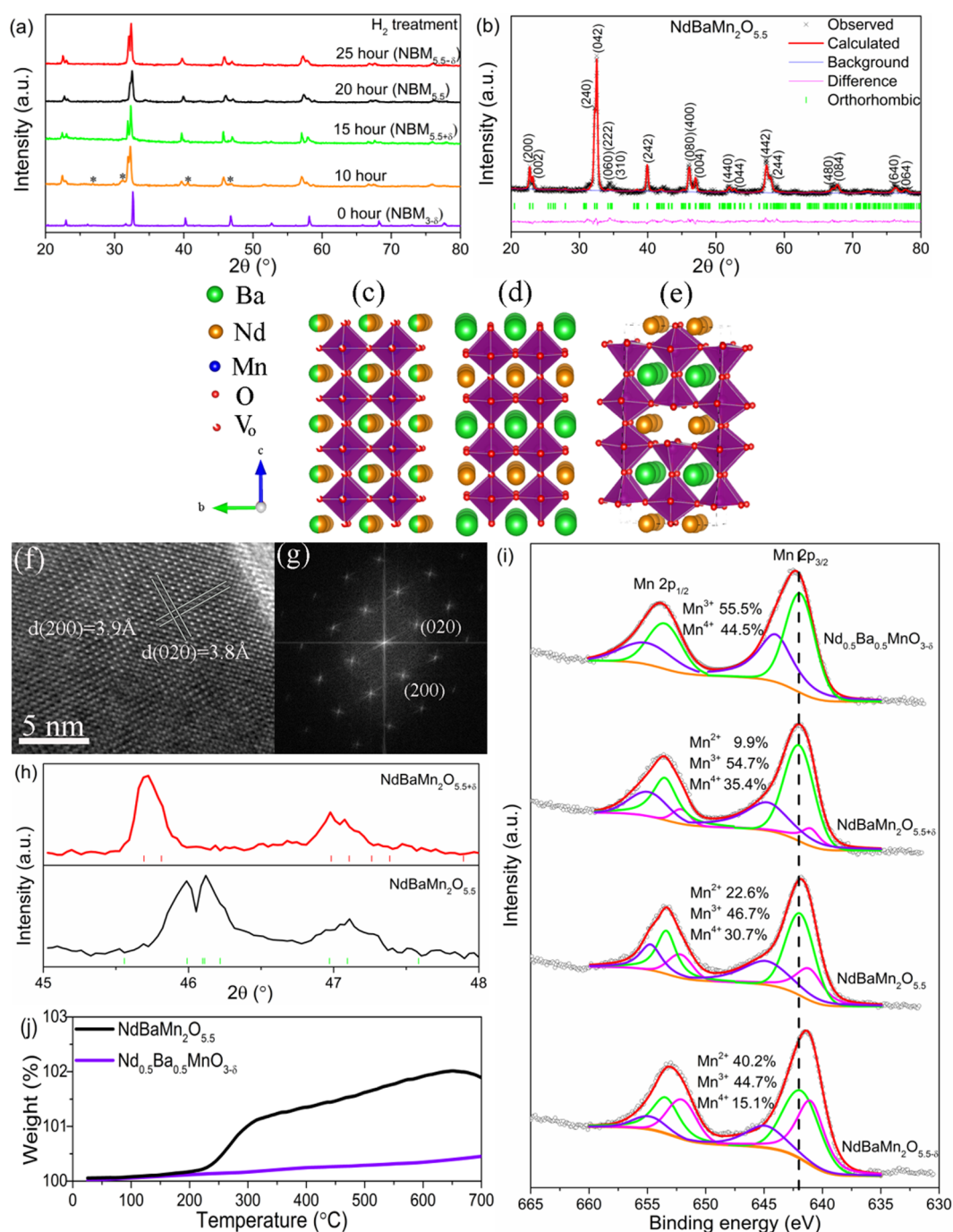
Figure 1. (a) XRD survey spectra of H_2-treated $NBM_{3-\delta}$ for 0, 10, 15, 20, and 25 h, where asterisks mark the secondary phases. (b) XRD refinement of $NdBaMn_2O_{5.5}$ (orthorhombic, *Icma*). Schematic illustrations of the crystal structures of (c) cubic NBM with disordered oxygen vacancies, (d) tetragonal NBM, where Nd−O and Ba−O layers alternate along the *c*-axis and the oxygen vacancies are localized in the Nd−O plane, and (e) orthorhombic $NBM_{5.5}$, where MnO_5 square pyramids and MnO_6 octahedra alternate along the *b*-axis. (f) High-resolution TEM image and (g) corresponding fast Fourier transform pattern of $NdBaMn_2O_{5.5}$. (h) Magnified X-ray diffraction patterns within the 2θ range of 45−48° for $NdBaMn_2O_{5.5+\delta}$ and $NdBaMn_2O_{5.5}$. (i) XPS fitting: experimental data (black circles), simulated spectrum (red line), background (orange line), Mn^{2+} (magenta line), Mn^{3+} (green line), and Mn^{4+} (violet line). (j) Thermogravimetric analysis of $Nd_{0.5}Ba_{0.5}MnO_{3-\delta}$, and $NdBaMn_2O_{5.5}$ in air.

former approach, one can substitute elements into the perovskite framework,[14] adjust the electronic configuration,[15,16] tune the strain,[17] and decorate the perovskite with nanoparticles.[18] The extrinsic methods resort, instead, to increasing the number of active sites by nanostructuring,[19] particle size reduction,[20] and porous structure construction.[21] Because of the approaches described above, perovskites have achieved significant progress as catalysts for H_2O oxidation.[22] Notably,

Shao-Horn and co-workers demonstrated that an optimal OER activity could be obtained by perovskite oxides with an approximately half-filled e_g orbital, whose occupancy determines the binding strength of oxygen-related intermediates and thus the activity.[15] Following this activity descriptor, $Ba_{0.5}Sr_{0.5}Co_{0.8}Fe_{0.2}O_{3-\delta}$ (BSCF5582) was found to have an intrinsic activity higher than that of the state-of-the-art OER catalyst IrO_2. However, the Shao-Horn group has reported that

fast surface amorphization of BSCF5582 and the leaching of A-site cations into the electrolyte result in poor cyclic stability.[23] Double perovskites ($LnBaM_2O_{5+\delta}$, where Ln = lanthanides and M = Mn or Co) have displayed OER activity and stability substantially enhanced compared with those of simple perovskite oxides.[24,25] The enhancement can be linked to the location of their O 2p-band center neither too far from nor too close to the Fermi level.[24]

Even though many transition metal oxides have demonstrated promising HER activity,[3,26,27] few perovskite oxides are studied as HER or overall water splitting catalysts.[28,29] Recently, Shao and Liu et al. have reported that two simple perovskite oxides, i.e., $Pr_{0.5}(Ba_{0.5}Sr_{0.5})_{0.5}Co_{0.8}Fe_{0.2}O_{3-\delta}$[28] and $SrNb_{0.1}Co_{0.7}Fe_{0.2}O_{3-\delta}$,[29] are capable of moderate HER electrolysis. Layered perovskites are usually characterized by oxygen diffusion and surface exchange rates that are faster than those of simple perovskites.[30,31] Even though several works have reported low-dimensional perovskite oxides, including double,[32] Ruddlesden−Popper (RP),[33] and even quadruple perovskites,[34,35] as OER catalysts, to the best of our knowledge, layered perovskites have not been used yet in overall water splitting electrolysis. Moreover, upon investigation of a layered perovskite as an OER catalyst, a crucial factor previously overlooked is the role of oxygen vacancies. For example, more oxygen vacancies likely contribute to a higher oxygen electrolysis rate.[19,36,37] Additionally, the alteration of oxygen nonstoichiometry can incur the phase changes of the material.[32] The modification of the electronic configuration and band structure accompanying oxygen vacancy concentration cannot be ignored. All of the factors mentioned above will have a substantial impact on the performance of perovskite oxides as water-splitting electrocatalysts.

In this work, we report a novel layered perovskite oxide, i.e., $NdBaMn_2O_{5.5}$, as a bifunctional catalyst for overall water electrolysis. $NdBaMn_2O_{5.5}$ was prepared by reductively annealing in H_2 its disordered counterpart, i.e., $Nd_{0.5}Ba_{0.5}MnO_{3-\delta}$ ($NBM_{3-\delta}$, where $\delta < 0.25$). H_2 treatment is a method commonly used to prepare layered perovskite oxides.[30] Several previous works have shown that synthesis of Mn-based layered perovskite ($LnBaMn_2O_{5+\delta}$) requires a strongly reducing atmosphere and that air synthesis usually results in a disordered phase.[38−40] By controlling the annealing time, we obtained several distinct layered neodymium barium manganese oxides (NBMs) with different oxygen vacancy amounts, including $NdBaMn_2O_{5.5-\delta}$ ($NBM_{5.5-\delta}$, where $\delta < 0.5$), $NdBaMn_2O_{5.5}$ ($NBM_{5.5}$), and $NdBaMn_2O_{5.5+\delta}$ ($NBM_{5.5+\delta}$, where $\delta < 0.5$). For NBM oxides, their structures have been recently examined by in situ neutron diffraction.[41] In addition, some of these materials have been studied as electrodes for solid oxide fuel cells.[42] However, to the best of our knowledge, they have not yet been investigated for room-temperature water electrolysis. Those oxides are characterized by diverse crystal phases, electronic configurations, band structures, and lattice distortions and have, therefore, distinct OER and HER activities. $NdBaMn_2O_{5.5}$ exhibits the best overall water splitting performance. This high activity could be attributed to its approximately half-filled e_g orbit occupancy, optimized O p-band center neither too close nor too far from the Fermi level, and a distorted structure. In addition, we found that the OER and HER activities of the investigated perovskite oxides are correlated; i.e., the material with a higher OER activity is also more active in catalyzing HER.

2. RESULTS

2.1. Structural Characterization. Layered NBM oxides were prepared through a reductive annealing method in H_2. Figure 1a gives the X-ray diffraction (XRD) patterns of the H_2-treated $NBM_{3-\delta}$ with variable annealing times. We conducted Rietveld refinements to clarify their phase structures. The results are displayed in Figure 1b, Figure S1, and Tables S1−S4. The $NBM_{3-\delta}$ prepared by the conventional sol−gel method (without H_2 treatment, i.e., 0 h) is a mixture of 92 atom % cubic phase ($Pm\bar{3}m$, ICSD-155548) and 8 atom % hexagonal phase ($P63/mmc$, ICSD-23874) (see Figure S1a and Table S1). When the compound was annealed in pure H_2 for 20 h, an orthorhombic ($Icma$, ICSD-152235) phase was obtained for $NBM_{5.5}$ with the following lattice parameters: $a = 7.918$ Å, $b = 7.778$ Å, and $c = 15.871$ Å (see Figure 1b,e and Table S2). This determined phase for $NBM_{5.5}$ is consistent with the previous result obtained by in situ neutron diffraction.[41] During reduction, the partial removal of crystalline oxygen and increased oxygen vacancies ($2Mn^{\bullet}_{Mn} + O^{\times}_O \rightarrow {}^1/_2O_2 + V^{\bullet\bullet}_O + 2Mn^{\times}_{Mn}$) force the A-site cations to be ordered: the layers of Nd−O and Ba−O alternate along the c-axis, as shown schematically in panels d and e of Figure 1. The ordering of Nd^{3+} and Ba^{2+} leads to oxygen vacancies being preferentially localized in the Nd−O plane.[43] Several studies have demonstrated that the ordering of oxygen vacancies occurs for layered $LnBaM_2O_{5.5}$.[40,44,45] At this level of oxygen nonstoichiometry, MO_5 square pyramids and MO_6 octahedra alternate along the b-axis, as illustrated in Figure 1e. This atomic arrangement is further confirmed by our density functional theory (DFT) calculations. We have considered four kinds of atomic arrangements for $NBM_{5.5}$ (see Figure S2), and the structure in Figure 1e has the lowest ground state energy.

Figure 1f shows a representative high-resolution transmission electron microscopy (TEM) image of orthorhombic $NBM_{5.5}$, from which a high crystallinity and clear lattice fringes are observed. The fast Fourier transform (FFT) analysis in Figure 1g detects lattice spacings of 3.8 and 3.9 Å, corresponding to the (020) and (200) lattice planes, respectively, further confirming the orthorhombic structure of $NBM_{5.5}$. For $NBM_{5.5+\delta}$ and $NBM_{5.5-\delta}$, their lattice phases are determined to be tetragonal ($P4/mmm$, ICSD-150705) (see Figure S1b,c and Tables S3 and S4). This finding is consistent with the previous report that increasing or decreasing δ perturbs the vacancy ordering of $LnBaM_2O_{5.5}$ and results in a tetragonal phase with higher lattice symmetry.[40] The lower lattice symmetry of the orthorhombic phase for $NBM_{5.5}$ in comparison to that of the tetragonal phase can be reflected by the split doublet peaks at around $2\theta = 46°$,[41] as shown in Figure 1h.

Through iodometric titration, δ in disordered $NBM_{3-\delta}$ is determined to be 0.12, giving an average oxidation state of Mn ion of 3.26. As a consequence of reductive annealing in H_2, the oxygen vacancy amount per formula unit in the layered perovskite oxides increases as a function of time to 0.35, 0.54, and 0.8 for $NBM_{5.5+\delta}$, $NBM_{5.5}$, and $NBM_{5.5-\delta}$, respectively. The negative shift of the Mn 2p X-ray photoelectron spectroscopy (XPS) spectrum in Figure 1i also confirms that oxygen vacancies are added. In addition, the valence state of Mn on the surface obtained by XPS fitting generally agrees well with the bulk values determined by chemical titrations, e.g., the deconvolution of the Mn 2p core-level spectrum for $NBM_{5.5}$
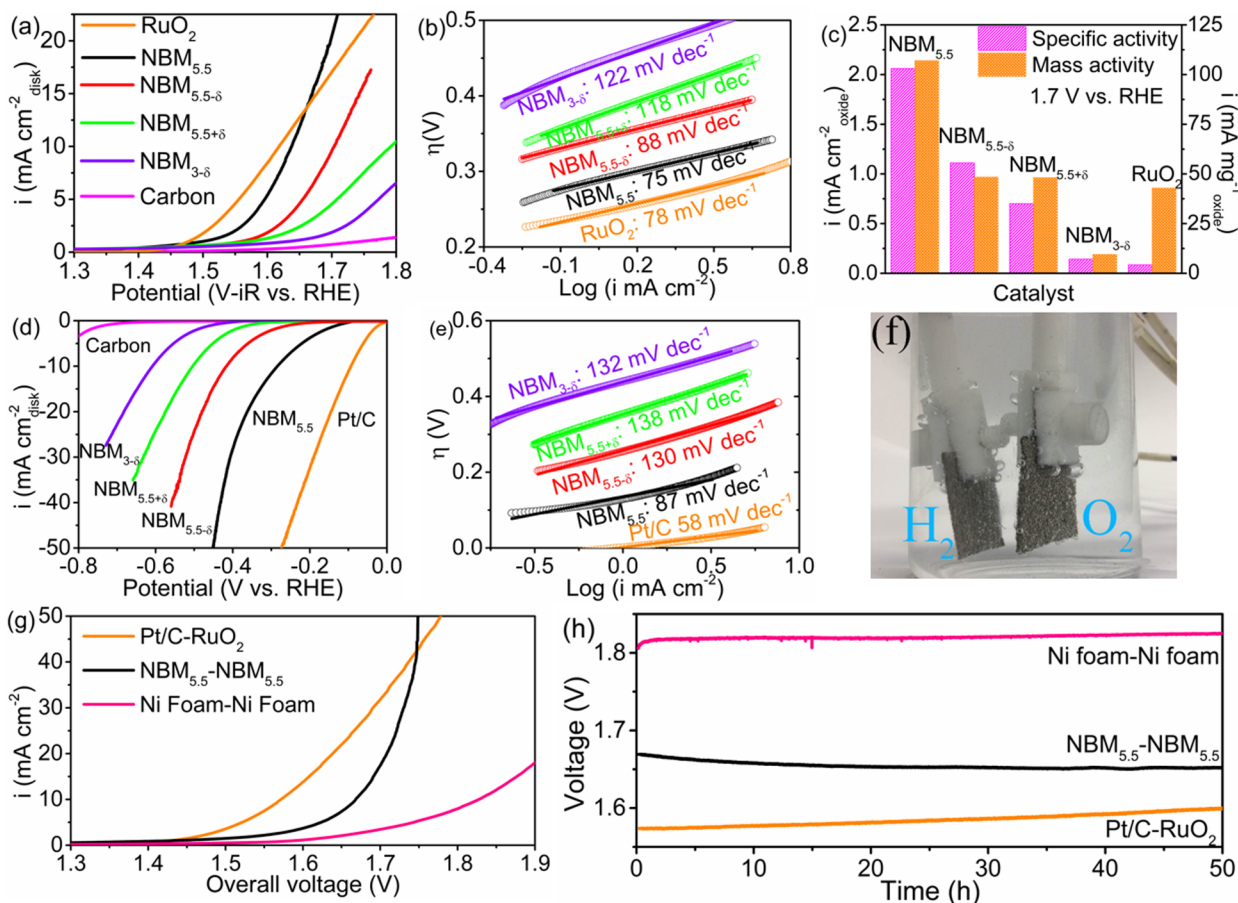
Figure 2. Catalytic performance evaluation. (a) OER LSV polarization curves and (b) corresponding Tafel plots. (c) Intrinsic and mass OER activities at 1.7 V vs the RHE. (d) HER LSV polarization curves and (e) corresponding Tafel plots. (f) Photo of a homemade water electrolyzer using $NBM_{5.5}-NBM_{5.5}$ as the electrode material. The generation of H_2 and O_2 bubbles at 10.0 mA cm^{-2} is clearly visible on Ni foam. (g) Polarization curves for overall water splitting catalysis. (h) Chronopotentiometry curves of $NBM_{5.5}-NBM_{5.5}$, Pt/C–RuO$_2$, and Ni foam–Ni foam at a constant current density of 10 mA cm^{-2}. All experiments were conducted in a 1 M KOH electrolyte.

suggests the presence of 22.6 atom % Mn^{2+}, 46.7 atom % Mn^{3+}, and 30.7 atom % Mn^{4+}. The estimated oxidation state of Mn is 3.08, a value very close to the value of 2.96 obtained from titration.

In Figure 1j, thermogravimetric analysis (TGA) conducted in air detects a mass increase starting from ∼200 °C for the investigated oxygen-deficient perovskite (this is in good agreement with a previous report[45]), and the mass increase can be attributed to the oxidation of Mn ions as well as the incorporation of lattice oxygen. In fact, many works have demonstrated that oxygen-deficient perovskite oxides are subjected to oxidation in an oxygen-rich environment.[30,33,46] In addition, it is worth noting that the magnitude of the weight gain is in a good agreement with their oxygen non-stoichiometry; e.g., an ∼1.8 wt % mass increase is observed in the testing temperature range for NBM$_{5.5}$, corresponding to an uptake of ∼0.5 oxygen per formula unit (NdBaMn$_2$O$_{5.5}$).

The morphology of the as-prepared materials can be assessed via scanning electron microscopy (SEM) (see Figure S3). The energy dispersive X-ray (EDX) mapping in Figure S4 reveals a homogeneous distribution of Nd, Ba, Mn, and O, with an atomic ratio qualitatively matching the target stoichiometry. From Figure S5, the Brunauer–Emmett–Teller (BET) specific surface areas among the investigated perovskites are similar and much smaller than that of the carbon support (Vulcan XC-72, S_{BET} = 236.4 m^2 g^{-1}).

2.2. Catalytic Activity. Each sample was loaded on a rotating disk electrode to evaluate its catalytic performance (mass loading of ∼0.4 mg cm^{-2}). We corrected all the potentials to be against the RHE (see Figure S6) using the equation E(RHE) = E(Ag/AgCl + 1.02 V).

We first studied the OER activity of the materials by linear sweep voltammetry (LSV) (see Figure 2a). Compared with that of disordered NBM$_{3-\delta}$, the onset potentials of all the layered perovskite oxides are shifted significantly to more negative potential regions, and the current densities at the same overpotentials are increased, suggesting an improved OER activity. It is worth noting that NBM$_{5.5}$ has the best performance among all the investigated perovskite oxides, and its current density at large overpotentials (e.g., η = 0.43 V) even exceeds that of commercial RuO$_2$. In particular, the Tafel slope of NBM$_{5.5}$ (75 mV decade^{-1}) is smaller than that of RuO$_2$ (78 mV decade^{-1}) (see Figure 2b), leading to an enhanced OER rate under slightly increased overpotentials. We also compared the mass (normalized by the oxide mass loading) and intrinsic (normalized by the BET surface area) OER activities,[47,48] as shown in Figure S7. Figure 2c compares the intrinsic and mass activity of all materials at 1.7 V versus the RHE. All studied perovskites have intrinsic activities higher than that of RuO$_2$ [S_{BET} = 50.8 m^2/g (see Figure S8)], demonstrating that NBM has a promising OER activity. Specifically, the activity of NBM$_{5.5}$ (2.06 mA/cm^2 of oxide) is ∼24 times higher than that

of the benchmark catalyst RuO_2 (0.084 mA/cm^2 of oxide). In addition, its mass activity (107 mA/mg of oxide) is ~2.5 times larger than that of RuO_2 (42.7 mA/mg of oxide). We should note that the activity of the commercial catalysts obtained in this work is consistent with several recent literature reports (see Table S5).

Figure 2d shows the HER polarization curves, which clearly show that the order of the HER activity for the investigated perovskite oxides is the same as that of their OER activities; i.e., $NBM_{5.5}$ is still the most active material, followed in sequence by $NBM_{5.5-\delta}$, $NBM_{5.5+\delta}$, and $NBM_{3-\delta}$. The substantially enhanced HER activity of $NBM_{5.5}$ is further confirmed by its much smaller Tafel slope (87 mV decade^{-1}) in comparison to that of the other perovskites (>130 mV decade^{-1}) (see Figure 2e). In addition, the overpotential needed by $NBM_{5.5}$ (0.29 V) to deliver a current density of 10 mA cm^{-2} is only 0.20 V larger than that of commercial Pt/C (0.09 V). It is important to note that the activity of $NBM_{5.5}$ is comparable to that of recently discovered state-of-the-art HER catalysts (see Table S6). We also investigated the catalytic durability of $NBM_{5.5}$. From panels a and b of Figure S9, it can be seen there is no obvious change in the OER and HER polarization curves after cyclic voltammogram (CV) scans for 2000 cycles, suggesting an excellent stability. In addition, $NBM_{5.5}$ is also examined by chronopotentiometry. From panels c and d of Figure S9, the voltage $NBM_{5.5}$ needs to achieve a current density of 10 mA cm^{-2} during HER and OER does not change significantly, confirming once again its good stability.

To evaluate the overall water splitting performance, we assembled a water electrolyzer working in a 1 M KOH electrolyte. We loaded the prepared samples on nickel foams that act as the support for both the anode and the cathode[49−54] (see Figure 2f). The contribution of nickel foam to the overall water splitting activity is small[55,56] (see Figure 2g), and the activity is consistent with previously reported literature data (see Table S7). The bubbles of H_2 and O_2 continuously generated during the electrolysis (10.0 mA cm^{-2}) are clearly visible. The evolution of generated H_2 and O_2 is also measured (see Figure S10). From the results, the amounts of generated gases are very close to the theoretical values, giving a faradaic efficiency of ~100%. From Figure 2g, even though the onset potential of $NBM_{5.5}$−$NBM_{5.5}$ is still more positive than that of the benchmark combination (Pt/C−RuO_2), the current density of $NBM_{5.5}$−$NBM_{5.5}$ exceeds that of Pt/C−RuO_2 when the applied voltage is >1.75 V. We should note that the obtained overall activity of $NBM_{5.5}$−$NBM_{5.5}$ is comparable to and even better than those of many state-of-the-art water splitting catalysts (see Table S7). In addition, we observe that $NBM_{5.5}$ exhibits a much better catalytic durability during the chronopotentiometry test than Pt/C−RuO_2 does. The overall voltage necessary for $NBM_{5.5}$−$NBM_{5.5}$ to achieve a 10 mA cm^{-2} current density displays activation,[57] which is then followed by a stable plateau at ~1.65 V. In contrast, after consecutive 50 h tests, Pt/C−RuO_2 suffers from obvious activity degradation,[58] with the corresponding voltage increasing by ~0.03 V. In addition, from the TEM photo and corresponding FFT patterns in Figure S11, the structure of $NBM_{5.5}$ is well maintained after the long chronopotentiometry tests, further confirming its excellent catalytic durability.

3. DISCUSSION

From the results presented above, $NBM_{5.5}$ has proven to be an exciting bifunctional OER and HER catalyst, substantially

surpassing the disordered $NBM_{3-\delta}$ as well as layered $NBM_{5.5+\delta}$ and $NBM_{5.5-\delta}$. Understanding what factors contribute to the enhancement could benefit the rational design of highly active water-splitting electrocatalysts. At present, the widely recognized OER mechanism on perovskite oxides in an alkaline electrolyte is called the adsorbate evolution mechanism (AEM)[59,60] (see Figure 3a). It begins with the adsorption of
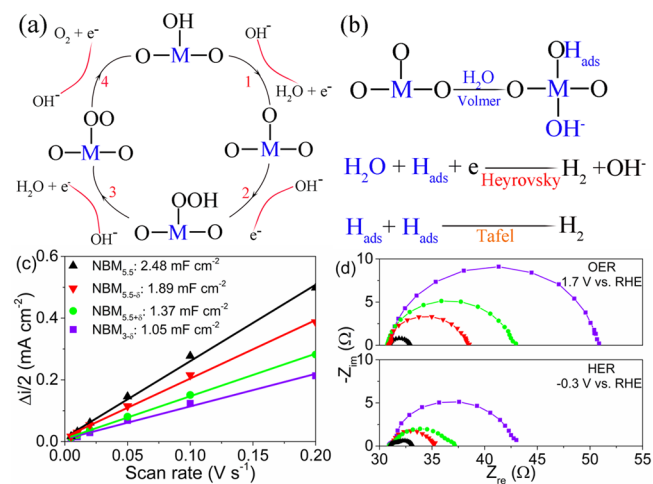
Figure 3. (a) Classic four-step adsorbate evolution mechanism for perovskite oxides. (b) Volmer−Tafel and Volmer−Heyrovsky processes for HER in an alkaline electrolyte. (c) Dependence of the capacitive current on the different potential scan rate. (d) EIS Nyquist plots for $NBM_{5.5}$ (black), $NBM_{5.5-\delta}$ (red), $NBM_{5.5+\delta}$ (green), and $NBM_{3-\delta}$ (violet). The spectra are recorded in the OER potential region of 1.7 V vs the RHE and the HER potential region of −0.3 V vs the RHE.[29]

OH^- onto the active site of perovskite, followed by the four elementary reaction steps involving the adsorption or desorption of a series of intermediates, including O*, OH*, and OOH* (the asterisk denotes the surface active site), where the formation of the OOH* intermediate is usually regarded as the rate-limiting step.[22] On the other hand, in a basic electrolyte, HER can happen through two different pathways, namely, the Volmer−Tafel and Volmer−Heyrovsky processes,[61,62] as shown in Figure 3b. Both processes comprise H_2O molecule adsorption, H_2O reduction generating H and OH^-, adsorption and desorption of OH^-, and formation of H intermediates for hydrogen evolution. During the Volmer reaction, the generated OH^- from H_2O reduction could preferentially attach to the transition metal site because of the electrostatic affinity, while the nearby O site could provide a site for H adsorption.[28,29] Recent work has demonstrated that the adsorption of OH^- rather than H_2O is a more important step in alkaline HER electrolysis.[3,28,63,64] In addition, the rate-limiting step of HER can be assessed from the slope of the Tafel plot. Slopes of ≈120, 40, and 30 mV decade^{-1} correspond to the Volmer, Heyrovsky, and Tafel reaction limitations, respectively.[3,61,65] From Figure 2e, the Tafel slope values for all the investigated catalysts are close to 120 mV decade^{-1}, suggesting that HER catalysis may be controlled by the Volmer process.

We acquired the electrochemical active surface area (ECSA) of the investigated materials via CV. From Figure S12, $NBM_{5.5}$ is characterized by a capacitive current that is much larger than those of $NBM_{3-\delta}$, $NBM_{5.5+\delta}$, and $NBM_{5.5-\delta}$. As shown in Figure

3c, the measured double-layer capacitance (the ECSA at the same loading mass) of NBM$_{5.5}$ is approximately 1.3−2.4 times higher than that of the other perovskites, suggesting a significantly increased active area. On the other hand, the electrochemical impedance spectra (EIS) are recorded to evaluate the charge transfer resistance during HER and OER. It can be seen from Figure 3d that NBM$_{5.5}$ has a charge transfer resistance that is much smaller than and correspondingly charge transfer kinetics significantly faster than those of the other materials. In the following sections, we consider e$_g$ filling, O p-band location, and structural distortions to explore the enhancements described above.

3.1. e$_g$ Filling. We first examine the e$_g$ orbital occupancy of the transition metal ions. Compared with the π-bonding t$_{2g}$ orbital, the σ-bonding e$_g$ orbital has a stronger overlap with the surface anion adsorbate. As a result, the filling of the e$_g$ orbital can substantially affect the binding of oxygen-related intermediates on the B-site cations and ultimately impact the electrocatalytic activity.[15] The valence states of the investigated NBM oxides are obtained by iodometric titrations, and the presence of both octahedral (O_h) and square pyramidal symmetry (C_{4v}) is considered, as illustrated in Figure 4a.
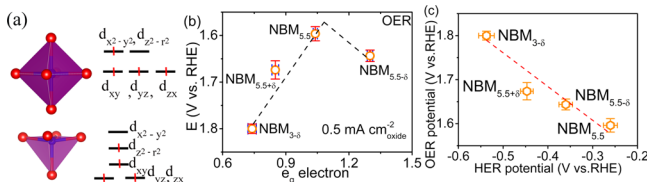
Figure 4. (a) Schematic representation of the octahedral and square pyramidal forms for Mn cations, with different electron distributions in the corresponding crystal-field split d-orbit. (b) Dependence of OER activity on the occupancy of the e$_g$ orbit. (c) Relationship between OER and HER activity, both of which are defined as the potential to deliver a current density of 0.5 mA/cm^2 of oxide. The error bar is the standard deviation calculated from three separate experiments. The dashed volcano line is displayed only for reference.

The dependence of OER activity (defined as the potential to deliver a current density of 0.5 mA/cm^2 of oxide)[24] on the occupancy of the e$_g$ orbit is displayed in Figure 4b. In the series of materials studied, the experiment suggests a volcano-shaped relationship between the 3d e$_g$ orbit occupancy and OER activity. Figure 4c further suggests that the investigated perovskite oxides have correlated OER and HER activities. This correlation is also supported by another activity indicator (HER and OER potential at 10 mA/cm^2 of disk) (see Figure S13). In fact, the charge transfer between the surface cation and adsorbed reaction intermediates is critical to both OER and HER electrolysis.[3,22,63] In particular, from the results described above, the Volmer process involving the adsorption of H$_2$O and OH$^-$ appears to be the rate-limiting step of HER. An optimized e$_g$ filling is suggested to promote such charge transfer between the surface cation and adsorbed reaction intermediates.[15] NBM$_{5.5}$, the most active one, has an optimal e$_g$ orbital filling close to unity (1.04). This is likely correlated to the smallest charge transfer resistance in Figure 3d.

3.2. O p-Band Structure. Besides e$_g$ filling, the relative positions of the oxygen p band and transition metal d band relative to the Fermi level are another important activity descriptor (shown schematically in Figure 5a). In contrast to the oxygen p band, DFT calculations of the transition metal
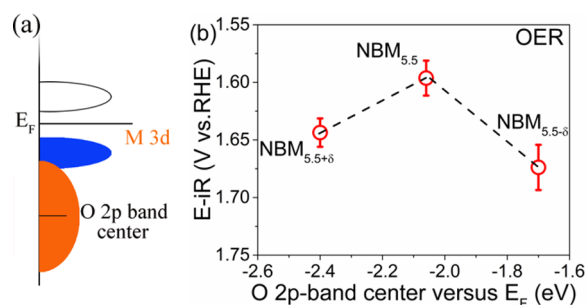
Figure 5. (a) Schematic illustration of the O 2p-band center of the perovskite oxide. (b) Dependence of OER activity on the O 2p-band center vs the Fermi level. The required potential at $i = 0.5$ mA/cm^2 of oxide is used to define OER activity. The O 2p-band center relative to E_F is obtained by DFT calculations, and the error bar stands for the standard divergence calculated from three different experimental tests. The dashed volcano line works only for reference.

cation d band potentially lead to a strong correlation error. As a result, only the position of the O p band is calculated to derive a more accurate picture of the electronic configuration for the investigated oxides.[24] From Figure 5b, the O p band of NBM$_{5.5}$ (−2.06 eV) with the highest activity is not too far from or close to the Fermi level, in contrast to those of NBM$_{5.5+\delta}$ (−2.40 eV) and NBM$_{5.5-\delta}$ (−1.70 eV). This configuration is beneficial for the hybridization and covalency of the O p band and transition metal d band, as well as the promotion of the charge transfer between the active redox center and adsorbed intermediates.[24] This could be another factor contributing to the decreased charge transfer resistance.

3.3. Structural Distortion. Figure 6 shows the lattice structures of different NBM perovskites. Upon closer
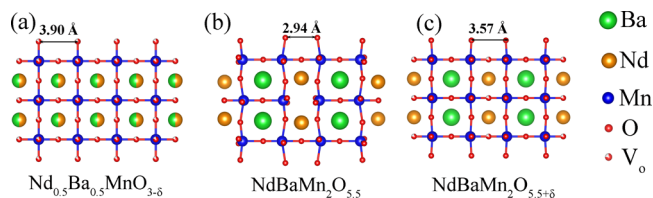
Figure 6. Projection along the [010] direction for (a) Nd$_{0.5}$Ba$_{0.5}$MnO$_{3−\delta}$, (b) NdBaMn$_2$O$_{5.5}$, and (c) Nd$_{0.5}$Ba$_{0.5}$MnO$_{5.5+\delta}$, showing different structural distortions and Mn environments.

examination, orthorhombic NBM$_{5.5}$ is characterized by a much larger structural distortion, consistent with the previous report.[41] This distorted structure of NBM$_{5.5}$ could be caused by the Jahn−Teller effect and ordering of the electronic orbital.[32,41] From the calculation results, the shortest oxygen−oxygen distance between two neighboring oxygen atoms connected to the nearest neighboring Mn ions is determined to be 2.94 Å. This value is much smaller than the corresponding distance in NBM$_{3−\delta}$ consisting of corner-shared octahedra (3.90 Å), as well as the one in tetragonal NBM$_{5.5+\delta}$ (3.57 Å). It is reported that, when the nearby oxygen−oxygen distance is <3 Å, it is possible for the oxygen atoms to interact with each other directly and form oxygen molecules.[34,35] The substantially reduced oxygen−oxygen distance likely contributes to the formation of bulk O−O species, thus promoting OER activity. The increased number of O−O species on the surface of NBM$_{5.5}$ can be assessed from the XPS fitting of the O 1s spectrum for the three materials,[28,29,47] as shown in Figure S14,

which detects a much larger proportion of O−O species formed on the surface of NBM$_{5.5}$ than on the other two materials.

In addition, a large number of square pyramids (see Figure 1e) are present in NBM$_{5.5}$. This kind of open structure in layered perovskite oxides can provide many more active sites for the adsorption of H_2O or OH^-,[32] two key species for OER and HER.[59−62] Ultimately, this could also contribute to the larger ECSA observed for NBM$_{5.5}$ in Figure 3c.

4. CONCLUSION

In this work, a facile reductive annealing method is used to obtain a series of layered perovskite oxides with variable oxygen vacancy amounts, lattice phases, electronic configurations, and structural distortions. A novel oxygen-deficient perovskite (NdBaMn$_2$O$_{5.5}$) structure is for the first time utilized as a bifunctional electrode material for overall water splitting. NdBaMn$_2$O$_{5.5}$ exhibits a substantially improved activity in catalyzing OER and HER, in comparison to those of its counterparts, including disordered Nd$_{0.5}$Ba$_{0.5}$MnO$_{3−\delta}$ and less distorted NdBaMn$_2$O$_{5.5+\delta}$ and NdBaMn$_2$O$_{5.5-\delta}$ ($\delta < 0.5$). The substantially enhanced performance could be attributed to the approximately half-filled e$_g$ orbit occupancy, optimized O p-band center location, and distorted structure. In addition, it is found that for the investigated perovskite oxides, OER and HER activities appear to be correlated. This work can serve as an important reference for perovskite oxides as water-splitting electrocatalysts.

■ ASSOCIATED CONTENT

Ⓢ Supporting Information

The Supporting Information is available free of charge on the ACS Publications website at DOI: 10.1021/acscatal.7b02650.

   Detailed experimental procedures and supplementary figures and tables (PDF)

■ AUTHOR INFORMATION

Corresponding Authors
*E-mail: francesco.ciucci@ust.hk.
*E-mail: dengjie.chen@jnu.edu.cn.

ORCID ⦿
Dengjie Chen: 0000-0002-3234-7020
Zongping Shao: 0000-0002-4538-4218
Francesco Ciucci: 0000-0003-0614-5537

Notes
The authors declare no competing financial interest.

■ ACKNOWLEDGMENTS

■ REFERENCES

(1) Seh, Z. W.; Kibsgaard, J.; Dickens, C. F.; Chorkendorff, I.; Nørskov, J. K.; Jaramillo, T. F. *Science* **2017**, *355* (6321), eaad4998.
(2) Wang, J.; Ciucci, F. *Small* **2017**, *13* (16), 1604103.
(3) Jin, H.; Wang, J.; Su, D.; Wei, Z.; Pang, Z.; Wang, Y. *J. Am. Chem. Soc.* **2015**, *137* (7), 2688−2694.
(4) Burke, M. S.; Enman, L. J.; Batchellor, A. S.; Zou, S.; Boettcher, S. W. *Chem. Mater.* **2015**, *27* (22), 7549−7558.
(5) Long, X.; Wang, Z.; Xiao, S.; An, Y.; Yang, S. *Mater. Today* **2016**, *19* (4), 213−226.
(6) Kibsgaard, J.; Chen, Z.; Reinecke, B. N.; Jaramillo, T. F. *Nat. Mater.* **2012**, *11* (11), 963−969.
(7) Jiang, P.; Liu, Q.; Liang, Y.; Tian, J.; Asiri, A. M.; Sun, X. *Angew. Chem., Int. Ed.* **2014**, *53* (47), 12855−12859.
(8) Liao, L.; Wang, S.; Xiao, J.; Bian, X.; Zhang, Y.; Scanlon, M. D.; Hu, X.; Tang, Y.; Liu, B.; Girault, H. H. *Energy Environ. Sci.* **2014**, *7* (1), 387−392.
(9) Zhong, Y.; Xia, X.; Shi, F.; Zhan, J.; Tu, J.; Fan, H. J. *Adv. Sci.* **2016**, *3* (5), 1500286.
(10) Qu, K.; Zheng, Y.; Jiao, Y.; Zhang, X.; Dai, S.; Qiao, S.-Z. *Adv. Energy Mater.* **2017**, *7*, 1602068.
(11) Jia, Y.; Zhang, L.; Gao, G.; Chen, H.; Wang, B.; Zhou, J.; Soo, M. T.; Hong, M.; Yan, X.; Qian, G.; Zou, J.; Du, A.; Yao, X. *Adv. Mater.* **2017**, *29* (17), 1700017.
(12) Lee, J. G.; Hwang, J.; Hwang, H. J.; Jeon, O. S.; Jang, J.; Kwon, O.; Lee, Y.; Han, B.; Shul, Y.-G. *J. Am. Chem. Soc.* **2016**, *138* (10), 3541−3547.
(13) Zhu, Y.; Zhou, W.; Sunarso, J.; Zhong, Y.; Shao, Z. *Adv. Funct. Mater.* **2016**, *26* (32), 5862−5872.
(14) Xu, X.; Su, C.; Zhou, W.; Zhu, Y.; Chen, Y.; Shao, Z. *Adv. Sci.* **2016**, *3* (2), n/a.
(15) Suntivich, J.; May, K. J.; Gasteiger, H. A.; Goodenough, J. B.; Shao-Horn, Y. *Science* **2011**, *334* (6061), 1383−1385.
(16) Suntivich, J.; Gasteiger, H. A.; Yabuuchi, N.; Nakanishi, H.; Goodenough, J. B.; Shao-Horn, Y. *Nat. Chem.* **2011**, *3* (7), 546−550.
(17) Petrie, J. R.; Jeen, H.; Barron, S. C.; Meyer, T. L.; Lee, H. N. *J. Am. Chem. Soc.* **2016**, *138* (23), 7252−7255.
(18) Gao, Y.; Wang, J.; Lyu, Y.-Q.; Lam, K.; Ciucci, F. *J. Mater. Chem. A* **2017**, *5* (14), 6399−6404.
(19) Zhao, B.; Zhang, L.; Zhen, D.; Yoo, S.; Ding, Y.; Chen, D.; Chen, Y.; Zhang, Q.; Doyle, B.; Xiong, X.; Liu, M. *Nat. Commun.* **2017**, *8*, 14586.
(20) Jung, J.-I.; Risch, M.; Park, S.; Kim, M. G.; Nam, G.; Jeong, H.-Y.; Shao-Horn, Y.; Cho, J. *Energy Environ. Sci.* **2016**, *9* (1), 176−183.
(21) Xu, J. J.; Xu, D.; Wang, Z. L.; Wang, H. G.; Zhang, L. L.; Zhang, X. B. *Angew. Chem., Int. Ed.* **2013**, *52* (14), 3887−3890.
(22) Chen, D.; Chen, C.; Baiyee, Z. M.; Shao, Z.; Ciucci, F. *Chem. Rev.* **2015**, *115* (18), 9869−9921.
(23) May, K. J.; Carlton, C. E.; Stoerzinger, K. A.; Risch, M.; Suntivich, J.; Lee, Y.-L.; Grimaud, A.; Shao-Horn, Y. *J. Phys. Chem. Lett.* **2012**, *3* (22), 3264−3270.
(24) Grimaud, A.; May, K. J.; Carlton, C. E.; Lee, Y.-L.; Risch, M.; Hong, W. T.; Zhou, J.; Shao-Horn, Y. *Nat. Commun.* **2013**, *4*, 2439.
(25) Chen, D.; Wang, J.; Zhang, Z.; Shao, Z.; Ciucci, F. *Chem. Commun.* **2016**, *52* (71), 10739−10742.
(26) Wang, H.; Lee, H. W.; Deng, Y.; Lu, Z.; Hsu, P. C.; Liu, Y.; Lin, D.; Cui, Y. *Nat. Commun.* **2015**, *6*, 7261.
(27) Yan, X.; Tian, L.; He, M.; Chen, X. *Nano Lett.* **2015**, *15* (9), 6015−6021.
(28) Xu, X.; Chen, Y.; Zhou, W.; Zhu, Z.; Su, C.; Liu, M.; Shao, Z. *Adv. Mater.* **2016**, *28* (30), 6442−6448.
(29) Zhu, Y.; Zhou, W.; Zhong, Y.; Bu, Y.; Chen, X.; Zhong, Q.; Liu, M.; Shao, Z. *Adv. Energy Mater.* **2017**, *7* (8), 1602122.
(30) Sengodan, S.; Choi, S.; Jun, A.; Shin, T. H.; Ju, Y.-W.; Jeong, H. Y.; Shin, J.; Irvine, J. T.; Kim, G. *Nat. Mater.* **2015**, *14* (2), 205−209.
(31) Pelosato, R.; Cordaro, G.; Stucchi, D.; Cristiani, C.; Dotelli, G. *J. Power Sources* **2015**, *298*, 46−67.
(32) Kim, J.; Yin, X.; Tsao, K.-C.; Fang, S.; Yang, H. *J. Am. Chem. Soc.* **2014**, *136* (42), 14646−14649.

(33) Takeguchi, T.; Yamanaka, T.; Takahashi, H.; Watanabe, H.; Kuroki, T.; Nakanishi, H.; Orikasa, Y.; Uchimoto, Y.; Takano, H.; Ohguri, N.; Matsuda, M.; Murota, T.; Uosaki, K.; Ueda, W. *J. Am. Chem. Soc.* **2013**, *135* (30), 11125−11130.

(34) Yamada, I.; Fujii, H.; Takamatsu, A.; Ikeno, H.; Wada, K.; Tsukasaki, H.; Kawaguchi, S.; Mori, S.; Yagi, S. *Adv. Mater.* **2017**, *29* (4), 1603004.

(35) Yagi, S.; Yamada, I.; Tsukasaki, H.; Seno, A.; Murakami, M.; Fujii, H.; Chen, H.; Umezawa, N.; Abe, H.; Nishiyama, N.; Mori, S. *Nat. Commun.* **2015**, *6*, 8249.

(36) Chen, C.-F.; King, G.; Dickerson, R. M.; Papin, P. A.; Gupta, S.; Kellogg, W. R.; Wu, G. *Nano Energy* **2015**, *13*, 423−432.

(37) Bao, J.; Zhang, X.; Fan, B.; Zhang, J.; Zhou, M.; Yang, W.; Hu, X.; Wang, H.; Pan, B.; Xie, Y. *Angew. Chem.* **2015**, *127* (25), 7507−7512.

(38) Taskin, A.; Lavrov, A.; Ando, Y. *Appl. Phys. Lett.* **2005**, *86* (9), 091910.

(39) Trukhanov, S.; Trukhanov, A.; Szymczak, H.; Szymczak, R.; Baran, M. *J. Phys. Chem. Solids* **2006**, *67* (4), 675−681.

(40) Kim, J.-H.; Manthiram, A. *J. Mater. Chem. A* **2015**, *3* (48), 24195−24210.

(41) Tonus, F.; Bahout, M.; Dorcet, V.; Gauthier, G. H.; Paofai, S.; Smith, R. I.; Skinner, S. J. *J. Mater. Chem. A* **2016**, *4* (30), 11635−11647.

(42) Pineda, O. L.; Moreno, Z. L.; Roussel, P.; Świerczek, K.; Gauthier, G. H. *Solid State Ionics* **2016**, *288*, 61−67.

(43) Ávila-Brande, D.; King, G.; Urones-Garrote, E.; Subakti; Llobet, A.; García-Martín, S. *Adv. Funct. Mater.* **2014**, *24* (17), 2510−2517.

(44) Frontera, C.; Caneiro, A.; Carrillo, A.; Oró-Solé, J.; García-Muñoz, J. *Chem. Mater.* **2005**, *17* (22), 5439−5445.

(45) Caignaert, V.; Millange, F.; Domenges, B.; Raveau, B.; Suard, E. *Chem. Mater.* **1999**, *11* (4), 930−938.

(46) Hua, B.; Zhang, Y. Q.; Yan, N.; Li, M.; Sun, Y. F.; Chen, J.; Li, J.; Luo, J. L. *Adv. Funct. Mater.* **2016**, *26* (23), 4106−4112.

(47) Liu, R.; Liang, F.; Zhou, W.; Yang, Y.; Zhu, Z. *Nano Energy* **2015**, *12*, 115−122.

(48) Zhu, Y.; Zhou, W.; Chen, Z. G.; Chen, Y.; Su, C.; Tadé, M. O.; Shao, Z. *Angew. Chem., Int. Ed.* **2015**, *54* (13), 3897−3901.

(49) Luo, J.; Im, J.-H.; Mayer, M. T.; Schreier, M.; Nazeeruddin, M. K.; Park, N.-G.; Tilley, S. D.; Fan, H. J.; Grätzel, M. *Science* **2014**, *345* (6204), 1593−1596.

(50) Ng, J. W. D.; García-Melchor, M.; Bajdich, M.; Chakthranont, P.; Kirk, C.; Vojvodic, A.; Jaramillo, T. F. *Nat. Energy* **2016**, *1*, 16053.

(51) Duan, J.; Chen, S.; Zhao, C. *Nat. Commun.* **2017**, *8*, 15341.

(52) Cai, G.; Zhang, W.; Jiao, L.; Yu, S.-H.; Jiang, H.-L. *Chem.* **2017**, *2* (6), 791−802.

(53) You, B.; Sun, Y. *Adv. Energy Mater.* **2016**, *6*, 1502333.

(54) You, B.; Jiang, N.; Sheng, M.; Bhushan, M. W.; Sun, Y. *ACS Catal.* **2016**, *6* (2), 714−721.

(55) Song, J.; Zhu, C.; Xu, B. Z.; Fu, S.; Engelhard, M. H.; Ye, R.; Du, D.; Beckman, S. P.; Lin, Y. *Adv. Energy Mater.* **2017**, *7* (2), 1601555.

(56) Shi, H.; Liang, H.; Ming, F.; Wang, Z. *Angew. Chem., Int. Ed.* **2017**, *56* (2), 573−577.

(57) Wang, H.; Lee, H.-W.; Deng, Y.; Lu, Z.; Hsu, P.-C.; Liu, Y.; Lin, D.; Cui, Y. *Nat. Commun.* **2015**, *6*, 7261.

(58) Zhao, S.; Huang, J.; Liu, Y.; Shen, J.; Wang, H.; Yang, X.; Zhu, Y.; Li, C. *J. Mater. Chem. A* **2017**, *5* (8), 4207−4214.

(59) Hong, W. T.; Risch, M.; Stoerzinger, K. A.; Grimaud, A.; Suntivich, J.; Shao-Horn, Y. *Energy Environ. Sci.* **2015**, *8* (5), 1404−1427.

(60) Rong, X.; Parolin, J.; Kolpak, A. M. *ACS Catal.* **2016**, *6* (2), 1153−1158.

(61) Gao, X.; Zhang, H.; Li, Q.; Yu, X.; Hong, Z.; Zhang, X.; Liang, C.; Lin, Z. *Angew. Chem., Int. Ed.* **2016**, *55* (21), 6290−6294.

(62) Zhu, Y. P.; Liu, Y. P.; Ren, T. Z.; Yuan, Z. Y. *Adv. Funct. Mater.* **2015**, *25* (47), 7337−7347.

(63) Gong, M.; Zhou, W.; Tsai, M.-C.; Zhou, J.; Guan, M.; Lin, M.-C.; Zhang, B.; Hu, Y.; Wang, D.-Y.; Yang, J.; Pennycook, S. J.; Hwang, B.-J.; Dai, H. *Nat. Commun.* **2014**, *5*, 4695.

(64) Lu, Q.; Hutchings, G. S.; Yu, W.; Zhou, Y.; Forest, R. V.; Tao, R.; Rosen, J.; Yonemoto, B. T.; Cao, Z.; Zheng, H.; Xiao, J. Q.; Jiao, F.; Chen, J. G. *Nat. Commun.* **2015**, *6*, 6567.

(65) Vrubel, H.; Hu, X. *Angew. Chem.* **2012**, *124* (51), 12875−12878.